Soil Dynamics and Earthquake Engineering 179 (2024) 108520

Contents lists available at ScienceDirect

Soil Dynamics and Earthquake Engineering

journal homepage: www.elsevier.com/locate/soildyn

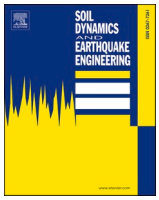

State-based assessment of cyclic liquefaction manifestation

Jorge Macedo *, Luis Vergaray

Civil and Environmental Engineering Department, 790 Atlantic Dr NW, Georgia Institute of Technology, Atlanta, GA, 30332, USA

A B S T R A C T

This study assesses the robustness of a framework based on critical state soil mechanics (CSSM) principles in evaluating earthquake-induced liquefaction manifestation. The assessment is motivated by the contrasting procedures in evaluating static and cyclic liquefaction, where mechanical properties commonly inform the former, whereas the latter often relies on semiempirical-based methods. The framework discussed in this study considers as ingredients (1) laboratory-based mechanical properties that are an average representation of soil's microstructure, (2) state inversion, (3) the link of state with cyclic resistance ratio (*CRR*), and (4) the seismic demand, represented by the cyclic stress ratio (*CSR*). The framework is assessed using ~5000 cone penetration tests (CPTus) conducted after the Canterbury earthquake sequence, where each CPTu is associated with liquefaction manifestation levels. The discussed framework is used to estimate safety factors, which are then combined with several liquefaction severity indexes (LSIs) to evaluate liquefaction manifestation in the context of a classification problem (i.e., "Yes" and "No"). The framework's performance is assessed using machine learning by estimating receiver operating characteristic curves (ROC). Different state inversion procedures are also considered, and recommendations based on their performance are provided. In particular, a calibrated cavity expansion-based inversion for New Zealand is proposed. We find that the discussed framework offers comparable performance to state-of-practice procedures, even when general considerations for mechanical properties based on CSSM are made, which is encouraging. Moreover, by including mechanical properties, it can better inform extrapolations for regions without significant data and non-typical soils as long as adequate properties are considered. In this context, it shares conceptual similarities with non-ergodic approaches in earthquake engineering.

1. Introduction

Static and cyclic (earthquake)-induced liquefaction have caused significant infrastructure damage, human losses, and environmental impacts. Notable examples of recent static liquefaction failures are the 2015 Fundao and 2019 Feijao tailings storage facility (TSF) failures in Brazil [1,2] and the Edenville-Sanford dam failure in 2020 [3]. The potential damage of earthquake-induced liquefaction has also been well documented after recent major earthquakes (e.g., the Canterbury earthquake sequence in New Zealand, the Kahramanmaraş Earthquake Sequence in Turkey) with several contributions (e.g., Ref. [4–11]). Interestingly, although liquefaction ubiquitously involves excess pore pressure, the frameworks for assessing static and cyclic liquefaction are different. Static liquefaction is commonly assessed under a mechanistic-based approach where parameters that average out micromechanical descriptors are measured in the laboratory and used along cone penetration testing (CPTu) data, with the link provided by the critical state soil mechanics (CSSM) framework. The critical state framework originated as an approach for avoiding liquefaction almost a century ago [12], with subsequent development over the following fifty years (by many contributors) to a theory of soil behavior: CSSM. CSSM has come to widespread use in the past decade for static liquefaction assessments, largely driven by the mining industry, where challenging materials (i.e., soils with unusual properties) such as mine tailings exist. In particular, CSSM proved necessary for forensic studies after recent TSF failures (e.g., Ref. [1,2,13]).

Cyclic liquefaction is commonly associated with earthquake-induced ground motions (although it is not exclusive to earthquakes, for example, storm-wave loading of offshore structures), with triggering primarily evaluated using semiempirical-based approaches that follow the seminal work of Seed and Idriss [14]. State-of-practice procedures use case history-based resistance curves (often estimated from standard penetration tests – SPT, cone penetration tests – CPTu, or shear wave velocity measurements) to separate liquefaction from no-liquefaction. The seismic demand is quantified by the cyclic stress ratio (*CSR*), often expressed in terms of the peak ground acceleration (*PGA*), and the resistance is quantified by the cyclic resistance ratio (*CRR*), which is, in turn, derived from the aforementioned case history-based resistance curve. *CRR* is corrected for overburden stress, but soil properties only appear as a further correction using the notion of fines content. The *CSR* and *CRR* are used to estimate a depth-dependent safety factor as $FS = CRR/CSR$, which is then used as an engineering input. Several variants of this framework, albeit with the original essence of the Seed and Idriss [14] procedure, have been proposed over the years (e.g., Ref. [15–18]).

* Corresponding author. Civil and Environmental Engineering Department, 790 Atlantic Dr NW, Georgia Institute of Technology, Atlanta, GA, 30332, USA.
E-mail address: jorge.macedo@gatech.edu (J. Macedo).

https://doi.org/10.1016/j.soildyn.2024.108520
Received 6 June 2023; Received in revised form 20 December 2023; Accepted 28 January 2024
Available online 16 February 2024

The essence of the Seed and Idriss [14] procedure (including subsequent variants) considers that soil properties are tacitly assumed to be indexed by fines content. In this context, some limitations of state-of-practice semi-empirical procedures are that (1) the databases used in regressing *CRR* curves have considered mainly sands and silty sands, with the bulk of the data having fine contents less than ~30 %, soil behavior index [19] $I_c < 2.25$ and effective vertical stresses ($\sigma_v^{'}$) up to ~200 kPa, as illustrated by Fig. 1, modified from Boulanger and Idriss [18], and (2) there is no direct link with mechanical parameters, which is in contrast with the common practice in static liquefaction assessments.

Given the limitations of semi-empirical procedures, it is intriguing to consider linking the cyclic resistance to soil properties and state. In this context, this study discusses a CSSM-based framework for assessing earthquake-induced liquefaction, focusing on liquefaction triggering and manifestation. The framework incorporates mechanical properties similar to those used in static liquefaction assessments, addressing limitations in traditional procedures. The framework's performance in the context of state-of-practice procedures is assessed using a machine learning technique and a large database (~10 000 observations) with liquefaction/no-liquefaction manifestation labels after the Canterbury earthquake sequence. In assessing the framework, different inversion options to estimate state - the state parameter, ψ, defined by Been and Jefferies [20], is used to represent state - are also evaluated, and a calibrated cavity expansion-based inversion for New Zealand is proposed.

This study is organized as follows: after providing the general background and motivations in the introduction (Section 1), Section 2 presents the considered liquefaction severity indexes (LSIs) for assessing liquefaction manifestation. Section 3 presents the CSSM-based framework discussed in this study and its ingredients (i.e., mechanical properties, CPTu-based state inversion, and state-based *CRR* estimation). Section 4 details the considered liquefaction New Zealand database. Section 5 presents the results of the framework assessment sharing insights. A discussion concerning different inversion options (including a calibrated option for New Zealand) follows in Section 6. Finally, the study closes by presenting conclusions and recommendation for future work in Section 7.

2. Liquefaction triggering and severity indexes

Once a *FS* profile is calculated for a site, liquefaction severity indexes (LSI) can be used to describe the potential of liquefaction manifestation – LSI, which amounts to weighting the *FS* by proportion through depth at the site. Examples of LSIs developed in the literature are the liquefaction potential index (*LPI*, - [21,22]), the Ishihara-inspired liquefaction potential index (LPI_{ish} - [23]), the liquefaction severity number (*LSN* - [9, 24]; LSN_{ish}[25]). In this study, *LPI*, LPI_{ish}, and *LSN* are used.

Equation (1) shows the general functional form structure used in estimating LSI, where $F(FS,\theta)$ is a function of *FS* and other θ parameters (e.g., the thickness of the non-liquefiable crust, H_1), and $w(z)$ is a depth (z)-dependent weighting factor. The steps for calculating different LSI indexes are similar. First, the *FS* profile is calculated using a liquefaction triggering procedure (often the procedures discussed in the previous section); then, LSI-specific parameters are estimated; and finally, the LSI operating equation is applied. An LSI derives in a scalar for a given soil profile, which can be used to differentiate liquefaction from no-liquefaction manifestation. For instance, previous efforts (e.g., Ref. [21,23,26–29]) have suggested thresholds of $LPI = 5-15$, $LPI_{ish} = 5$ and $LSN = 10-20$ for liquefaction manifestation assessments.

$$LSI = \int_0^z F(FS,\theta)w(z)dz \tag{1}$$

$F(FS,\theta)$ typically receives inputs from a liquefaction triggering procedure. For instance, (FS,θ) is a function of *FS* in *LPI*, *FS* and H_1 in LPI_{ish}, and *FS* and volumetric strains (ε_v) in *LSN*. Table 1 shows the functional form of F and $w(z)$ for different LSIs.

3. Mechanistic-based assessment of liquefaction triggering

This section presents the different ingredients for the framework used in this study for assessing cyclic-induced liquefaction triggering.

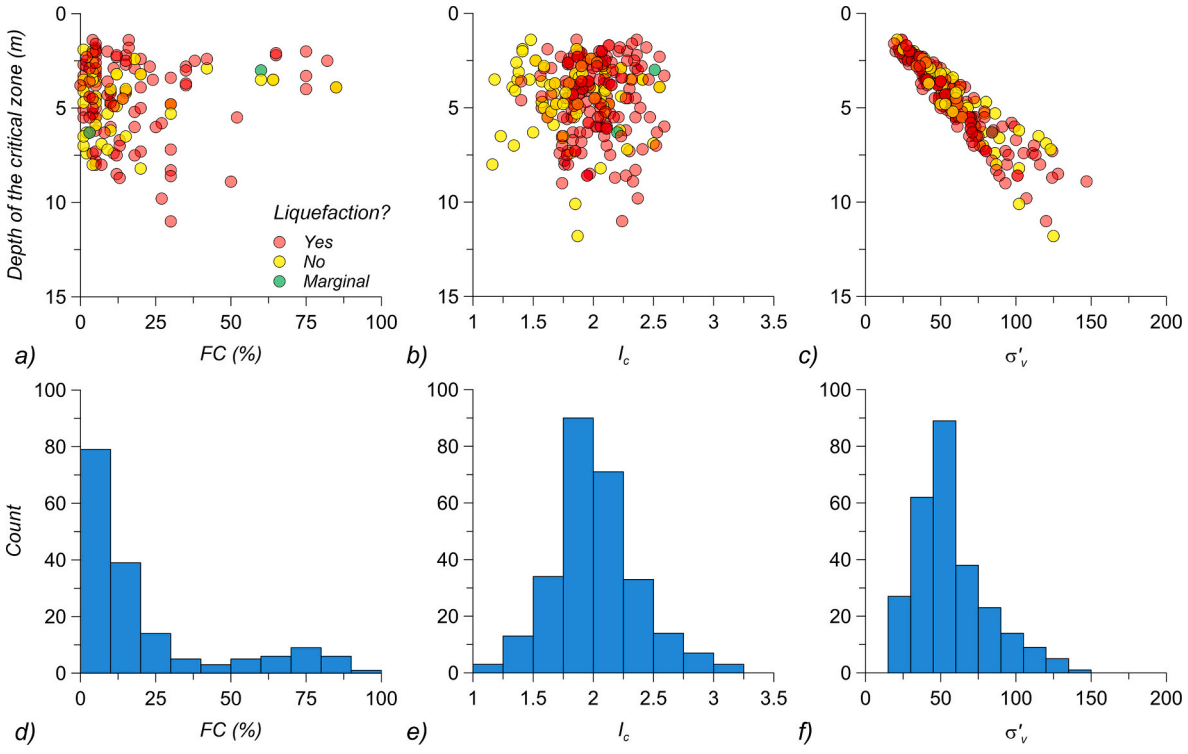

Fig. 1. Case histories in Boulanger and Idriss [18]. a) Fine contents, b) I_c, and c) $\sigma_v^{'}$ versus depth. Histograms of d) fine contents, f) I_c, and g) $\sigma_v^{'}$.

Table 1
Functional form of F and w for different LSIs.

LSI	$F(FS,\theta)$	$w(z)$
LPI	$1-FS, if\ FS \le 1$ $0, otherwise$	$10-0.5z$
LPI_{ish}	$\begin{cases} 1-FS, if\ FS \le 1 \cap H_1 m(FS) \le 3 \\ 0, otherwise \end{cases} m(FS) = e^{\left(\frac{5}{25.56(1-FS)}\right)} - 1$	$25.56/z$
LSN	ε_v	$1/z$

The framework benefits from previous CSSM-based efforts (e.g., Ref. [30]) that are more commonly used in static liquefaction assessments. As previously discussed, triggering is commonly conducted by estimating a safety factor as CSR/CRR. In the considered framework, CRR is related to mechanical parameters that can be measured and ψ, which can be estimated through a CPTu-based state inversion. CSR, which represents the demand part, is estimated based on the NCEER procedure [31] as $CSR = 0.65\frac{PGA}{g}\frac{\sigma_v}{\sigma_v'}r_d$, where σ_v is the total vertical stress, σ_v' is the effective vertical stress, g is the gravity, and r_d is a depth reduction factor estimated according to Ref. [18]. The following subsections elaborate on the ingredients of the discussed framework, including the considered mechanical parameters, the concept of CPTu-based state inversion, and the link between CRR and ψ, also accounting for mechanical parameters.

3.1. Mechanical parameters

The following mechanical parameters, often used in static liquefaction assessments, are considered in this study: (1) critical state line (CSL) parameters, including the CSL slope (λ_e), and its altitude (Γ), defined in Eq. (2), where e_{cs} is the void ratio at the critical state, and p_{cs}' is the mean effective stress at the critical state (the "cs" subscript stands for critical state); (2) the stress ratio at the critical state, $M_{tc} = \left(\frac{q}{p}\right)_{cs}$ (q is the deviatoric shear stress and "tc" stands for triaxial compression) and the volumetric coupling (N), which are related through stress-dilatancy as indicated by Eq. (3), where $\eta_{max} = (q/p')_{max}$ is the maximum shear stress ratio and $D_{min} = \left(\frac{d\varepsilon_v}{d\varepsilon_q}\right)_{min}$ is the maximum dilatancy, $d\varepsilon_v$ and $d\varepsilon_q$ are the volumetric and deviatoric strain rates; (3) the state-dilatancy parameter (χ), which relates D_{min} and ψ through Eq. (4); and (4) the stiffness-confinement dependence parameters (A, B) – Eq. (5). Γ, λ_e, M_{tc}, N, χ, are commonly estimated using triaxial tests, and A, and B can be estimated from bender elements or geophysical tests. Fig. 2 illustrates how these properties are commonly estimated from triaxial and bender tests using materials tested in the past by the authors and published in Macedo and Vergaray [32].

Even though derived from a macro scale response (i.e., triaxial tests), these parameters are intrinsically related to particle-level properties and the distribution of particle sizes. For instance, As discussed by Jefferies and Been [30] and Macedo and Vergaray [32], M_{tc} is a function of the particle shape and mineralogy, Γ is associated with the state dependence at low stresses, λ_e and N provide information on compressibility, χ is a kinematic parameter related to the dilation potential. Moreover, Vergaray et al. [33] elaborated on the dependence of CSL parameters (Γ and λ_e) and particle size distributions that promote packing. These parameters are derived under CSSM concepts (i.e., Equations (1)–(5)) and can be assessed for a range of soils, including sands, silts, and clays [34]. In applying the critical state approach, the notion of 'fines content' is

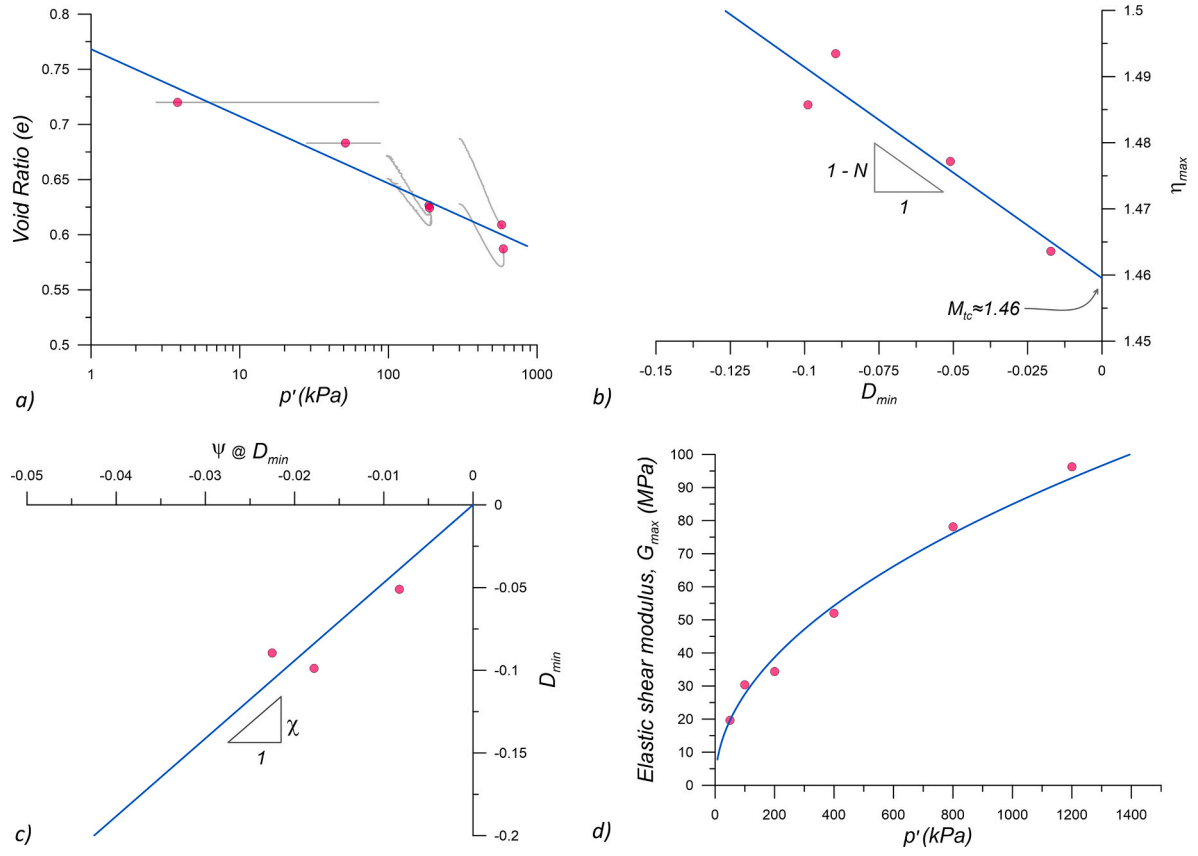

Fig. 2. Illustration of the estimation of mechanical-based parameters commonly used in static liquefaction assessments. a) CSL estimation, b) η_{max} versus D_{min} plot to estimate M_{tc} and N, c) state-dilatancy relationship to estimate χ, and d) G_{max} versus p' plot to estimate A and B. Information on plots (a), (b), and (c) is based on triaxial tests, and plot (d) is based on bender tests.

replaced by the soil's intrinsic friction (e.g., M_{tc}) and its compressibility (e.g., λ_e); moreover, a critical state approach has no concept of 'sand-like' or 'clay-like' behavior, as different soils simply exhibit different mechanical properties (e.g., M_{tc}, λ_e).

$$e_c = \Gamma - \lambda_e \ln p' \tag{2}$$

$$\eta_{max} = M_{tc} + (1 - D_{min})N \tag{3}$$

$$D_{min} = \chi\psi \tag{4}$$

$$G_{max} = A.F(e).\left(\frac{p'}{p_a}\right)^B \tag{5}$$

3.2. CPTu-based state inversion

The in-situ characterization of nonplastic soils depends largely on penetration tests such as CPTu tests. In a CPTu, the soil response (i.e., resistance) to an enforced displacement is measured through parameters such as the tip resistance (q_t), sleeve friction (f_s) and pore pressures (u_2). However, the engineer is ultimately interested in the properties/state of the soil. Recall that this study uses ψ to define state. This is an inverse problem, which can be expressed by Equation (6) [35], where Q is a normalized tip resistance ($Q = (q_t - p)/p'$). Note that Equation (6) also includes H, the plastic modulus, which can be related to λ for general estimations [30].

$$\psi = f(Q, G_{max}, M_{tc}, N, H, \chi, \Gamma, \lambda, p') \tag{6}$$

Equation (6) indicates that ψ can be estimated from CPTu measurements and the mechanical properties discussed in the previous section if the function f is known. There have been several efforts with different degrees of complexity in providing f. For instance, calibration chamber tests have been used to investigate the relationship between ψ and CPTu measurements. According to Jefferies and Been [30], approximately 15 sands with defined CSLs, and mechanical properties have been tested in calibrating chambers. In interpreting data from calibration chambers, Been et al. [36] proposed the functional form in Equation (7) for the inversion of state, which is a potential solution for the inversion problem.

$$\psi = \frac{-\ln Q/k}{m} \tag{7}$$

Where Q is measured in calibration chamber tests for a known ψ to find terms k and m, which are are material-specific constants and, as such, are functions of other intrinsic properties discussed in the previous section. Hence, in general, it can be stated that:

$$k = g(G_{max}, M_{tc}, N, H, \chi, \Gamma, \lambda) \tag{8}$$

$$m = h(G_{max}, M_{tc}, N, H, \chi, \Gamma, \lambda) \tag{9}$$

Where g and h are functions to be determined. Using the trends observed on calibration chamber tests, several studies [37–39] proposed screening procedures to estimate ψ. These procedures estimate k and m from the CSL's slope, which in turn is inferred from CPTu measurements and M_{tc}, i.e., g and h are reduced to functions that depend on λ and M_{tc}. Robertson [40] also proposed a procedure to estimate ψ directly from $Q_{tn,cs}$, a normalized version of the CPTu tip resistance corrected by fine contents. Other researchers have also used a combination of mini calibration chambers and miniature cones (e.g., Ref. [41–43]) to investigate the relationship between ψ and CPTu measurements. Shuttle and Jefferies [35] proposed a more elaborated method based on spherical cavity expansion analyses, which was later updated by Ghafghazi and Shuttle [44], Shuttle and Jefferies [45], and Mozaffari and Ghafghazi [46]. In cavity expansion-based methods, k_{sce} and m_{sce} (notice subscript "*sce*" indicates spherical cavity expansion) can be estimated through Eq. (10) and Eq. (11), where the functions f_1 to f_{12} depend on the mechanical parameters described in the previous sections. f_1 to f_{12} in Equations (10) and (11) are provided by Jefferies and Been [30] based on an extensive dataset of calibration chamber tests. Mozaffari and Ghafghazi [46] also provide alternative functional forms to Equations (10) and (11).

$$k_{sce} = \left(f_1\left(\frac{G_{max}}{p'}\right) f_2(M) f_3(N) f_4(H) f_5(\lambda) f_6(\nu)\right) \tag{10}$$

$$m_{sce} = \left(f_7\left(\frac{G_{max}}{p'}\right) f_8(M) f_9(N) f_{10}(H) f_{11}(\lambda) f_{12}(\nu)\right) \tag{11}$$

When the functional forms that control the inversion (i.e., Equations (10) and (11)) are based on cavity expansion simulations, the results are not representative of field conditions. In this context, mapping factors (summarized in Ref. [30]) to related cavity expansion simulations and field measurements have also been proposed, according to Eq. (12).

$$Q_{field} = c_1 (Q_{sce})^{c_2} \tag{12}$$

Where Q_{field} represents the field normalized tip resistance and Q_{sce} represents the cavity expansion-based normalized tip resistance and c_1, c_2 are mapping factors (see Table 2) that relate the k and m from cavity expansion (i.e., k_{sce} and m_{sce}) with k and m factors representative of field conditions (i.e., k_{field} and m_{field}) through Eq. (13). As discussed in subsequent sections, this study also provides calibrated mapping factors for New Zealand.

$$k_{field} = c_1 {k_{sce}}^{c_2} \text{ and } m_{field} = m_{sce} c_2 \tag{13}$$

Shuttle and Jefferies [45] proposed mapping coefficients dependent on ψ, but after some mathematical manipulations (Appendix A), it can be proven that they are equivalent to ψ independent coefficients. Even though the Robertson [40] procedure is not explicitly formulated as having the functional form of Equation (7), after some mathematical manipulations, it can be demonstrated that the procedure is also consistent with the general inversion form in Equation (7) (see Appendix B). The procedure proposed by Mozaffari and Ghafghazi [46], which provides inversion equations consistent with Eq. (8) and Eq. (9), does not include mapping factors as it is based on Arbitrary Lagrangian Eulerian (ALE) numerical simulations of the CPTu penetration that captured reasonably well the observed ψ in calibration chambers.

3.3. State-based *CRR* estimation

Once ψ is estimated from CPTu data and laboratory tests, *CRR* can be linked to ψ by using case histories where ψ is available (e.g., Ref. [30, 48]) or by relating *CRR* and ψ through laboratory tests, which would conceptually follow the procedures Upadhyaya et al. [49]. For the purposes of this study, the $CRR - \psi$ curve suggested by Jefferies and Been [30], which Macedo et al. [48] also used to assess liquefaction in the Harbor Bay area after the 1989 Loma Prieta earthquake, was used. This curve can be represented by Eq. (14), and it is based on 29 Class A case histories from Moss [50] interpreted by Jefferies and Been [30].

$$CRR = 0.06e^{-9\psi} \tag{14}$$

Recall that ψ in this equation can be estimated from CPTu data and mechanical properties. The analyses presented in the next sections consider different state-inversion options (Table 2), assessing them in the context of Geyin et al. [51] database. In terms of liquefaction triggering, once *CRR* is estimated from Eq. (14), *FS* can be estimated as commonly done, i.e., $FS = CRR/CSR$.

4. Liquefaction manifestation database

This study relies on the liquefaction database established by Geyin et al. [51], comprising approximately ~15 000 CPTu-based liquefaction case histories. These cases span 5668 distinct sites, each associated with

Table 2
State inversion equations considered in this study.

Inversion Equation	m or m_{sce}	k or k_{sce}	Scaling expressions	Mapping factors	Reference
Direct methods					
$\psi = -\frac{\ln\left(\frac{Q}{k}\right)}{m}$	$m = 11.9 - 13.3\lambda_{10}$ $\lambda_{10} = F_r/10$	$k = \left(3 + \frac{0.85}{\lambda_{10}}\right) M_{tc}$	–	–	Plewes et al. [38] – PL92
$\psi = -\frac{\ln\left(\frac{Q}{k}\right)}{m}$	$m = 11.9 - 13.3\lambda_{10}$ $\lambda_{10} = \frac{1}{34 - 10 \bullet I_{c-BJ}}$	$k = \left(3 + \frac{0.85}{\lambda_{10}}\right) M_{tc}$	–	–	Been and Jefferies [39] (1)
$\psi = -\frac{\ln\left(\frac{Q_{m.cs}}{k_R}\right)}{m_R}$ $\psi \approx -\frac{\ln\left(\frac{Q}{k}\right)}{m}$	$m = m_R = \sim 7$	$k_R \approx 50$ $k \approx \frac{3k_R}{2k_c}\left(\frac{P_a}{\sigma'_v}\right)^{1-n}$	–	–	Robertson [40] (App. B) – R10 (3)
Numerical based (cavity expansion and ALE based)					
$\psi = -\frac{\ln\left(\frac{Q}{k}\right)}{m}$	Eq. 10	Eq. 11	$k = c_1 k_{sce}{}^{c_2}$ $m = m_{sce} c_2$	$c_1 = 1.0$ $c_2 = 1.45$	Shuttle and Jefferies [35] – SJ98
				$c_1 = 0.7$ $c_2 = 1.7$	Ghafghazi and Shuttle [44] – GS08
			$k = c_k\, k_{sce}$ $m = m_{sce} + c_m$	$c_k = 3.2$ $c_m = 2.4$	Shuttle and Jefferies [45] (2) (App. A)
	Eq. 8	Eq. 9	–	–	Mozaffari and Ghafghazi [46] – MG23

Note: (1) I_{c-BJ} is the soil behavior index proposed by Been and Jefferies [39], (2) c_k and c_m are optimization parameters defined in Shuttle and Jefferies [45] with values of 3.2 and 2.4. (3) k_c is a factor that modifies the normalized tip resistance as function of I_c, defined by Ref. [19], and n is a factor that introduces a soil type dependence on the normalized tip resistance, as defined by Ref. [47]- see Appendix B.

three earthquake events from the Canterbury earthquake sequence (CES). The CES is characterized by three significant earthquakes: the Mw 7.1 Darfield Earthquake in September 2010, the Mw 6.2 Christchurch Earthquake in February 2011, and the Mw 5.7 Valentine's Day Earthquake in February 2016. The groundwater table (GWT) depth at each CPTu site is obtained from time-dependent models (van Ballegooy et al., 2014b), and the PGA – required in liquefaction assessments - is estimated using the Bradley [52] method. The database also has information on liquefaction manifestation severity, considering six different classes based on Green et al. [53] and summarized in Table 3. The database was filtered to exclude sites with CPTu recordings of less than 10 m depth so representative LSIs are estimated, sites where lateral spreading was observed at least in one of the events as it could affect the manifestation observations, and cases where the manifestation is unknown. The filtered database used in this study has ~10 000 observations, which are presented in Fig. 3, considering selected variables from the database; in addition, Fig. 4 shows the location of the considered sites. It can be noted that the Mw 7.1 Darfield and Mw 5.7 Valentine's Day earthquakes generated low PGA values and did not trigger liquefaction in most cases. Conversely, the Mw 6.2 Christchurch Earthquake caused larger PGA values and a more uniform distribution of different manifestation levels, including severe liquefaction cases.

Table 3
Liquefaction manifestation classification (adapted from Ref. [51]).

Classification Criteria	ID	Criteria
None	0	No surficial liquefaction manifestation or lateral spread cracking
Minor liquefaction	1	Small, isolated liquefaction features; streets had traces of ejecta or wet patches less than a vehicle width; <5 % of the ground surface was covered by ejecta
Moderate liquefaction	2	Groups of liquefaction features; streets had ejecta patches greater than a vehicle width but were still passable; 5 %–40 % of the ground surface was covered by ejecta
Severe liquefaction	3	Large masses of adjoining liquefaction features, streets impassible due to liquefaction, >40 % of the ground surface was covered by ejecta
Lateral spreading	4	Ejection of liquefied material at the ground surface may be observed, but lateral spreading is the predominant manifestation and damage mechanism. Measured crack-displacement widths are less than 200 mm.
Sever lateral spreading	5	Ejection of liquefied material at the ground surface may be observed, but lateral spreading is the predominant manifestation and damage mechanism. Measured crack-displacement widths exceed 200 mm
Unknown	10	Insufficient information to reliably classify: out of bounds, no reliable documentation, and obscured or otherwise ambiguous imagery

5. CSSM-based liquefaction manifestation assessment

Liquefaction manifestation will be considered as a classification problem with a specific instance in the database being tagged as having manifestation (i.e., a "Yes" case) or not (i.e., a "No" case). Specifically, when the severity index in Table 3 was 0, the entry was classified as "No"; when the severity index was higher or equal to 1, the entry was classified as "Yes." This criterion is also consistent with previous efforts [25–27,49,54–56]. Once the problem is set as a classification problem, the performance of different triggering procedures combined with LSIs can be assessed in terms of the proportion of identified true positive rates (*TPR*) and false positive rates (*FPR*). This assessment can be conducted using the receiver operating characteristic curve (ROC), which is a machine learning-based technique to assess the performance of binary classification methods [58]. ROCs have also been used in previous research for assessing liquefaction-triggering procedures [25,26,29,49,54–57,59,60].

Fig. 5 schematically shows how a ROC is estimated, considering the framework discussed in the previous section. In this illustrative example, the Robertson [40] equation (see Table 2) is used for the ψ inversion, and *LPI* is used as the *LSI*. The dashed lines in Fig. 5a represent different *LPI* thresholds that separate the "Yes" from "No" cases. Each considered threshold (e.g., points A to F) in Fig. 5a provides true positive (*TP*, cases that are correctly classified as liquefiable), false positives (*FP*, cases where liquefaction was not observed but incorrectly classified as liquefiable), true negatives (*TN*, cases where liquefaction was not observed and are correctly classified as non-liquefiable), and false negatives (*FN*, cases where liquefaction was observed but are incorrectly classified as non-liquefiable). These values that can then be used to calculate the $TPR = \frac{TP}{TP+FN}$ and $FPR = \frac{FP}{FP+TN}$ ratios plotted in Fig. 5b. In the context of soil liquefaction, *TPR* represents the proportion of correctly identified liquefiable cases, while *FPR* indicates the proportion of non-liquefiable

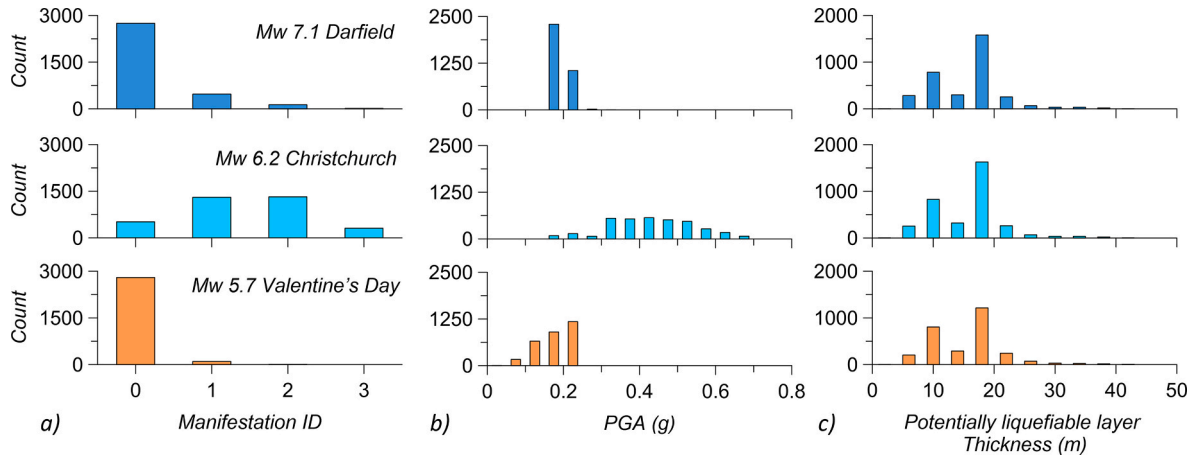

Fig. 3. Histograms of manifestation ID, b) PGA, and c) potentially liquefiable layer thickness of the database considered in this study.

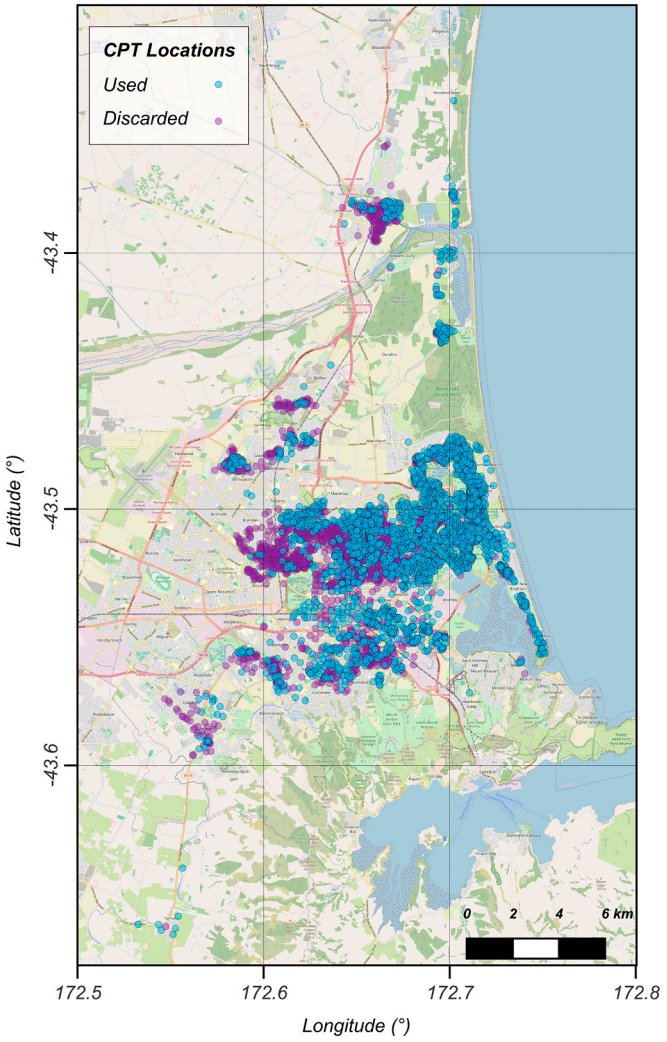

Fig. 4. Spatial distributions of sites considered in this study. "Used" refers to the sites considered after filtering. "Discarded" refers the filtered sites due to reasons discussed in the text.

cases incorrectly classified as susceptible. For instance, point A ($LPI = 2.7$) provides high *FPR* and high *TPR* values, as can also be inspected in Fig. 5a. In contrast, point E ($LPI = 18$) provides low *FPR* and *TPR* values. None of these cases are ideal. In this illustrative example, point C ($LPI = 8.7$) provides an adequate tradeoff between *FPR* and *TPR* as it is linked to the point on the ROC curve with the lowest *FPR* and highest *TPR*. This point is also known as the optimal operating point (OOP). Moreover, the closer the ROC curve is to the upper left corner, *TPR* increases, and *FPR* decreases, implying a better classification. In the extreme case of a perfect classifier, the area under the curve (AUC) in Fig. 5b will be 1. Thus, AUC can be used as an index to assess a classification method, with larger values (i.e., closer to 1) implying a better classification performance. In evaluating the framework discussed in this study, AUC values will be estimated for different scenarios and used in assessing performance. This is elaborated in the following.

5.1. Considered scenarios and evaluation steps

Seven scenarios, summarized in Table 4, were considered. Each scenario corresponds to an inversion option to estimate ψ, which is then used to estimate *CRR* as discussed previously. Note that the Shuttle and Jefferies [45] procedure in Table 2 is not considered as it is conceptually equivalent to the SJ98 and GS08 procedures. In estimating *CSR*, PGA is available in the database, σ'_0 and σ_0 are estimated from the water table location and CPTu-based unit weight estimates using the Robertson and Cabal [61] correlations and r_d is based on Boulanger and Idriss [18]. Once an *FS* profile is estimated, *LPI*, LPI_{ish} and *LSN*, are considered as the LSI metrics for assessing liquefaction manifestation. Then, the ROC curves based on *LPI*, LPI_{ish}, and *LSN*, are used to evaluate the performance of each scenario. Fig. 6 schematically illustrates the evaluation steps.

In the case of cavity expansion-based inversions, some assumptions are considered to estimate the required parameters directly from CPTu data. Specifically, M_{tc} was estimated considering a friction angle (φ) of 33. $I_c = 2.5$ was considered as the threshold for liquefaction, consistent with previous work done for New Zealand [49,57,60,62]. G_{max} was estimated as $G_{max} = V_s^2\rho$, where V_s is the shear wave velocity estimated from CPTu data based on the correlations developed by McGann et al. [63] for New Zealand. λ_{10} is estimated from the CPTu-based friction ratio ($\lambda_{10} = F_r/10$) when the Plewes et al. [38] method is used, and I_{c-BJ} for the Been and Jefferies [39] method (see Table 2). In other cases, λ_{10} is estimated using the Reid et al. [64] procedure. N is fixed as 0.3 and $\chi = 3.5$, which are typical for sands and silty sands [30], and H is estimated as $= 2/\lambda_e$, as recommended by Jefferies and Been [30] for sands and silty sands. The c_1 and c_2 scaling parameters that map cavity expansion results to field conditions were initially selected based on values reported in the literature (i.e., $c_1 = \{1, 0.7\}$ and $c_2 = \{1.45, 1.7\}$), and then optimized considering the database used in this study, as discussed in the next section. Lastly, the state-of-practice liquefaction triggering procedure of Boulanger and Idriss [18] – BI16 – is also used in estimating

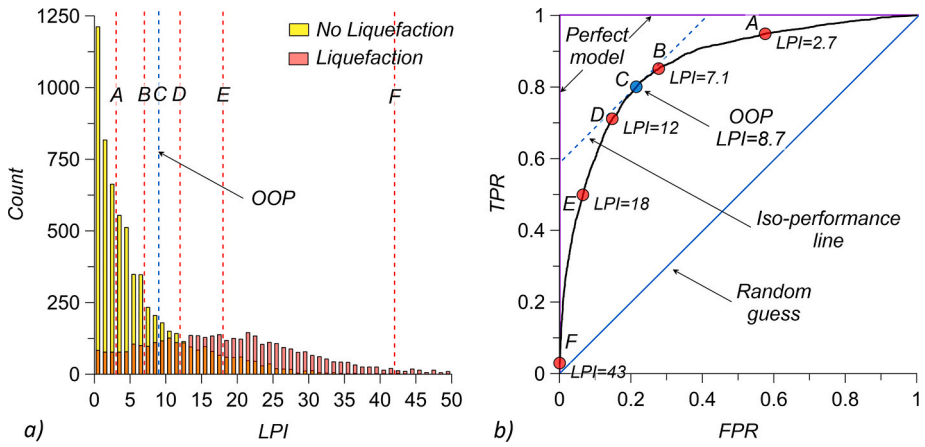

Fig. 5. ROC analyses: (a) distributions of liquefaction manifestation and no liquefaction manifestation as a function of *LPI*; (b) corresponding ROC curve, and illustration of how a ROC curve is used to assess the efficiency of a diagnostic test.

Table 4
Liquefaction manifestation classification (adapted from Ref. [51]).

Method	*LPI*		*LPI*$_{ish}$		*LSN*	
	AUC	OOP	AUC	OOP	AUC	OOP
BI16	0.890	4.5	0.877	3.6	0.859	11.3
R10	0.862	8.7	0.848	6.1	0.829	15.9
BJ92	0.851	0.7	0.819	0.1	0.852	2.5
PL92	0.841	1.1	0.812	0.5	0.838	2.9
SJ98	0.674	0.01	0.610	0.01	0.678	0.1
GS08	0.794	0.1	0.725	0.1	0.798	0.7
MG23	0.863	15.3	0.869	9.9	0.819	19.6
Optimized (This study) c_1 = 1.0, and c_2 = 1.9	0.870	13.2	0.876	8	0.835	18

AUC values with the database considered in this study for comparison purposes (next section). The fine contents estimate required in the Boulanger and Idriss [18] procedure is based on the Maurer et al. [62] correlation developed for New Zealand.

5.2. Results

Fig. 7 presents the ROC curves for *LPI*, *LPI*$_{ish}$ and *LSN*, considering the direct inversion ψ procedures (i.e., no numerical simulations involved in their formulation) R10, BJ92, and PL92. The ROC based on the BI16, considering a liquefaction probability of 16 %, consistent with previous efforts that estimated ROCs using BI16 [23,60], is also presented. The dispersion of ROC curves and AUC values are more pronounced when *LPI* and *LPI*$_{ish}$ are considered compared to the case where *LSN* is used. It can be observed that the R10 inversion provides ROC curves that are quite close to curves estimated using BI16 with AUC values that are also similar. The other direct inversion procedures (BJ92, PL92) also provide comparable ROC curves and AUC values (Table 4) as BI16. However, their OOPs are quite low (e.g., 0.7 and 1.1 for *LPI*), suggesting that they are unconservative, i.e., they tend to generate significantly low LSIs.

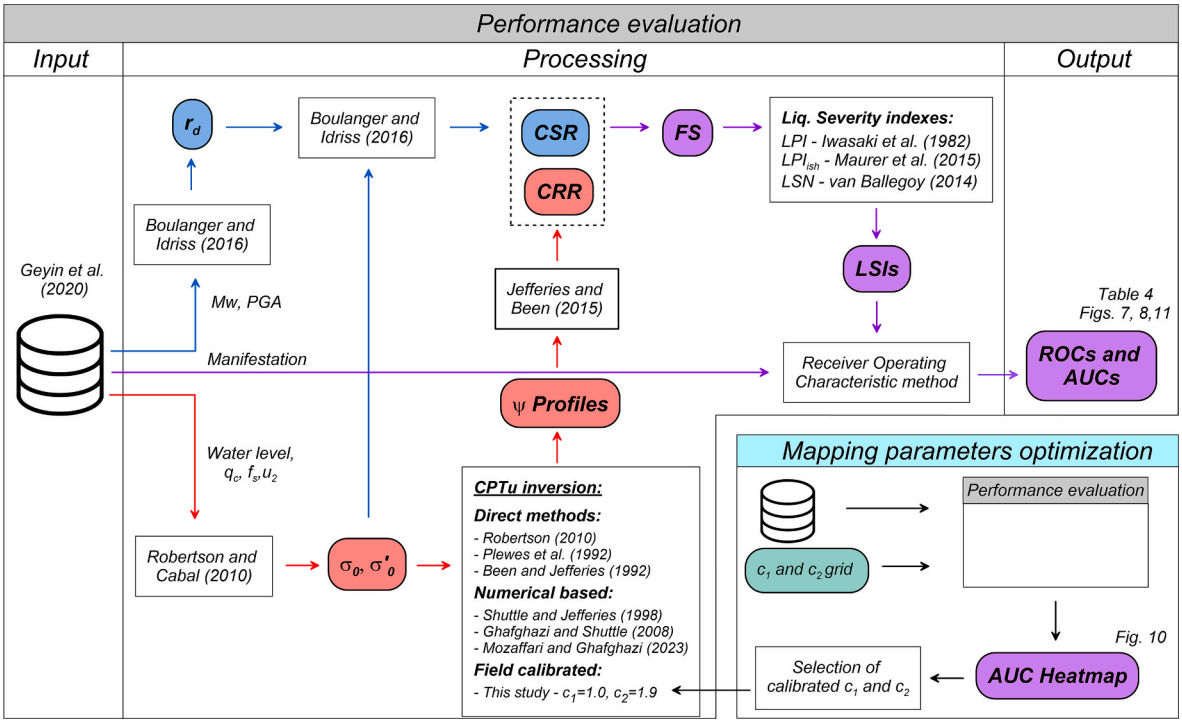

Fig. 6. Flow chart to assess cyclic liquefaction manifestation assessment procedures.

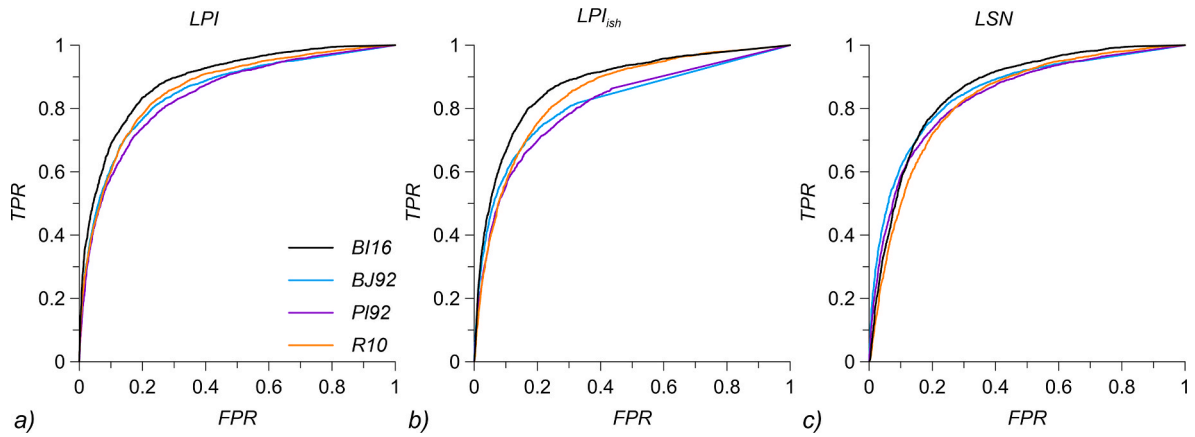

Fig. 7. a) *LPI*, b) LPI_{ish} and c) *LSN* ROC curves for direct ψ inversion procedures (R10, BJ92, and PI92) and the state-of-practice BI16 procedure.

The interesting result to highlight is that the framework discussed in this study with a simple inversion equation, i.e., R10, provides comparable performance to that of the state-of-practice BI16 procedure. Of note, as demonstrated in Appendix B, the R10 procedure can be approximated to an inversion equation implying constant m and variable k. Hence, the results suggest that these approximated m and k parameters are a reasonable representation of the average scaling of mechanical properties (i.e., Eq. (10) and (11)) for New Zealand soils in the context of the considered database. However, since Robertson's equation is not explicitly formulated in terms of mechanical properties (i.e., $G_{max}, M_{tc}, N, H, \chi, \Gamma, \lambda$), it is limited in terms of extrapolations.

Fig. 8 shows the results considering ψ inversion procedures that rely on numerical simulations (cavity expansion and ALE simulations). The results using BI16 and the R10 inversion are also shown for reference. The ALE-based MG23 procedure exhibits AUC values comparable to BI16 and the R10 inversion. In contrast, the cavity expansion-based approaches (SJ98, GS08) provide lower AUC values, and their OOPs are quite low (e.g., 0.01 and 0.1 for *LPI*), again suggesting they are unconservative (i.e., they tend to generate low LSIs). This can be attributed to the more sophisticated representation of the CPTu penetration process used by Mozaffari and Ghafghazi [46] in generating the data for the MG23 procedure, compared with cavity expansion analogies.

The cavity expansion-based results are dependent on the c_1, and c_2 mapping coefficients, with the GS08 inversion providing significantly larger AUC values than the SJ98 inversion (see Table 4). This might be because the c_1, and c_2 coefficients in the former were calibrated using a larger set of calibration chamber tests. On the other hand, the GS08 inversion has an inferior performance compared to the BI16 procedure, as noted by the significantly lower AUC values. A potential reason for this is that the c_1, and c_2 mapping coefficients suggested by Ghafghazi and Shuttle [44], even though representative of calibration chamber conditions, do not scale appropriately in the context of CPTu-based field liquefaction manifestation assessments in New Zealand. In this context, the c_1, and c_2 mapping coefficients were optimized based on AUC estimates for the New Zealand database, considering a grid of c_1 values from 0.1 to 3.0, and c_2 values from 0.5 to 4.0. For each c_1 and c_2 combination, ψ is inverted from CPTu data and used to estimate AUC values, following the procedures discussed in the previous section (Fig. 6). Fig. 9 illustrates how different c_1, and c_2 value results in different proportions of "Yes"/"No" cases, hence providing different TPR/FPR and AUC values.

The optimization results are presented in Fig. 10 as c_1/c_2 dependent AUC contours considering *LPI*, LPI_{ish}, and *LSN*. The c_1 and c_2 values for the cavity expansion-based procedures in Table 2 are also presented for reference. It can be observed that whereas the c_1 values for the procedures in Table 2 are consistent with the values observed in the highest AUC regions, the c_2 values need to be increased. In selecting c_1 and c_2, additional constraints were imposed by adding iso-OPP *LPI*, LPI_{ish}, and *LSN* lines (the blue lines in Fig. 10), considering ranges of LSI thresholds previously reported for New Zealand (e.g. Ref. [23,25,26,26–28,60]), i.e., $LPI = 5-15$, $LPI_{ish} = 5-10$, and $LSN = 10-20$. In the case of LPI_{ish}, there are less reported values compared to the other LSIs, thus a value of 10 for the upper range was considered. Finally, the c_1 and c_2 values were selected considering the regions within the OPP lines that also maximize the AUC values and have a c_1 coefficient in the range reported by previous efforts. A range of c_2 values can result in similar

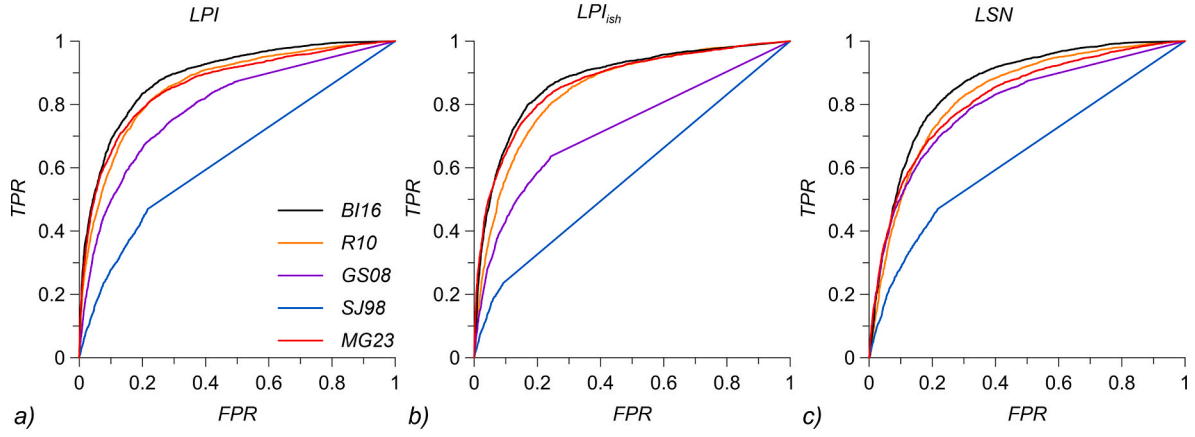

Fig. 8. a) *LPI*, b) LPI_{ish} and c) *LSN* ROC curves for ψ inversion procedures that rely on numerical simulations (cavity expansion – GS08, SJ98; and ALE simulations – MG23). Curves for the R10 inversion and BI16 procedure are also presented.

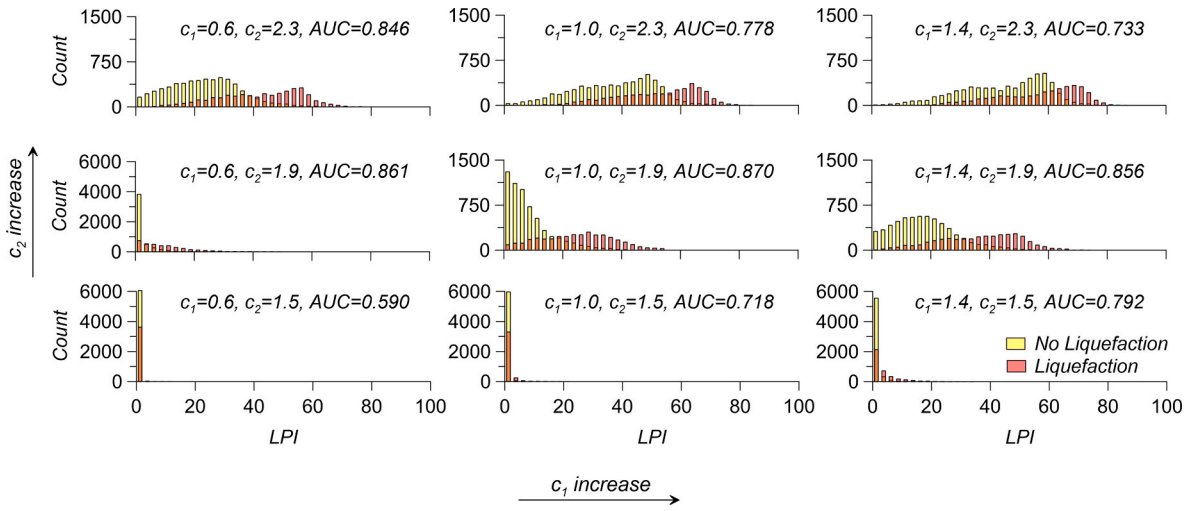

Fig. 9. Histograms of liquefaction and non-liquefaction manifestation for LPI considering varying c1(rows) and c2 (columns). LPI-based AUSE values are also presented for reference.

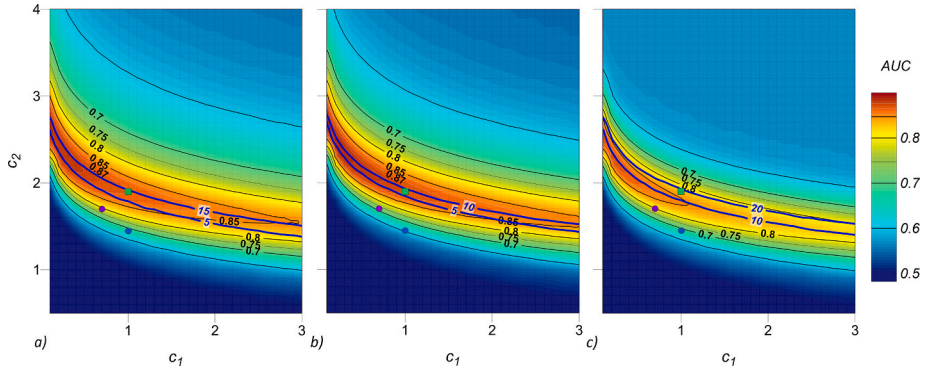

Fig. 10. AUC variation with c_1 and c_2 parameters for a) *LPI*, b) LPI_{ish} and c) *LSN*. The dots represent c_1 and c_2 pairs reported by Shuttle and Jefferies [35] and Ghafghazi and Shuttle [44]; the squares represent the optimized c_1 and c_2 values in this study.

AUCs for a given c_1. For example, the c_1 values provided by the procedures in Table 2 (e.g., $c_1 = 0.7$, 1) could be selected with c_2 pairs that result in high AUC values (e.g., $c_2 = 2.1$, 1.9). The combination $c_1 = 1$ and $c_2 = 1.9$ was opted for selection to imply only an exponential term in mapping cavity expansion results, as suggested by Shuttle and Jefferies [35]. A slightly higher AUC could be obtained for a lower c_1, but this could result in an optimal LPI_{ish} lower than 5 under minimal AUC improvement (<0.03), and LPI_{ish} was constrained to be higher than 5. Because of this and the previous discussions, $c_1 = 1$ and $c_2 = 1.9$ was maintained as the final selection. Fig. 11 shows the updated ROC curves using the calibrated c_1 and c_2 coefficients for New Zealand. It can be observed now that the performance is quite comparable to that of the BI16, MG23, and R10 procedures. The AUC values for the optimized c_1 and c_2 coefficients are presented in Table 4 with values 0.88 (LPI_{ish}), 0.87 (*LPI*), and 0.84 (*LSN*). These high AUC values indicate good performance; indeed, they are higher than other inversion methods and

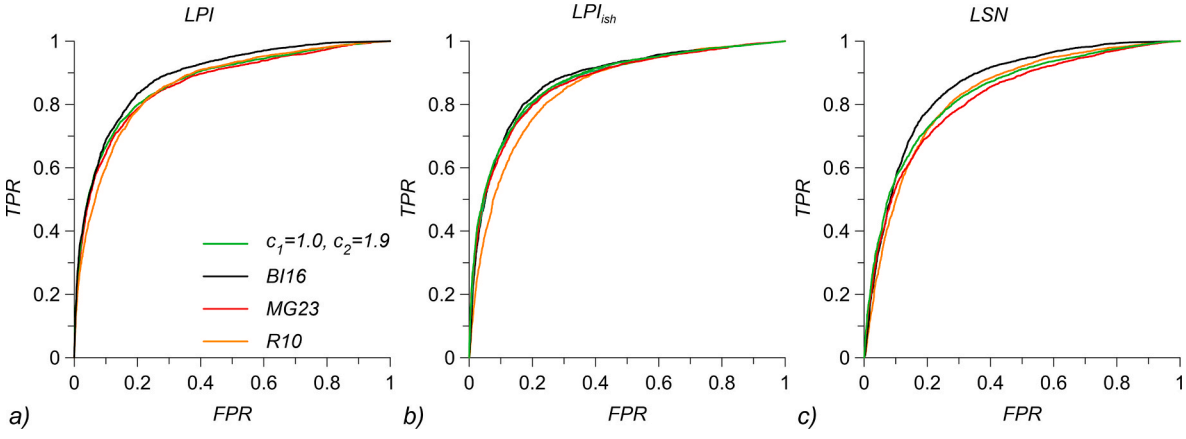

Fig. 11. a) *LPI*, b) LPI_{ish} and c) *LSN* ROC curves for BI16, R10/MG23 inversions, and the calibrated cavity expansion procedure.

quite close to the BI16 values. Thus, the calibrated c_1 and c_2 coefficients better capture the mapping of cavity expansion results to assess liquefaction manifestation in New Zealand (in an average sense) using CPTu data and are recommended as an alternative to existing cavity expansion-based inversion methods.

6. Discussion

It is interesting to see that in the context of the New Zealand liquefaction database used in this study, the performance of the Robertson [40] inversion procedure in assessing liquefaction manifestation is comparable to that of BI16, MG23, and the calibrated cavity expansion inversion in this study. Given the R10 inversion's simplicity and good performance, this may raise the question of why conducting a more complex calibration of cavity expansion mapping coefficients is necessary or even why using a more complex method such as the MG23 inversion would be required. The main motivation for this is that the calibrated cavity expansion-based and MG23 inversions allow for incorporating mechanical properties more directly (i.e., Equations (10) and (11)). The cavity expansion-based procedure recommended in this study could also be recalibrated for other regions if needed, following the steps in the previous section as far as data is available. Moreover, the computational cost for conducting cavity expansion-based simulations is significantly cheaper than the cost for ALE simulations (the basis for the MG23 procedure), making it more versatile if regional-based assessments are required. Lastly, it is also relevant to highlight that the good performance of the Robertson [40] inversion procedure, when used in conjunction with the framework discussed in this study, is because it generates LSI distributions that are comparable with those generated by the calibrated cavity expansion-inversion as illustrated by Fig. 12, considering *LPI*, LPI_{ish}, and *LSN*.

It is also relevant to highlight that in this study, only one $CRR - \psi$ curve was considered based on the suggestions by Jefferies and Been [30]. The considered curve was not trained with New Zealand data; however, it resulted in high AUC values, comparable to the AUCs from BI16, which considered New Zealand data. This suggests that the considered $CRR - \psi$ is reasonable in average terms for New Zealand, but this aspect should be further explored. In addition, future efforts could also evaluate the influence of "true liquefaction" curves, informed by cyclic laboratory data, as suggested by Upadhyaya et al. [49]. Lastly, data from calibration chambers are available for "well known" sands (e.g., Ticino, Ottawa, etc.) but not for Christchurch soils. Given the relevance of the New Zealand case histories for liquefaction engineering, calibration chamber data for representative Christchurch soils would be beneficial in gaining additional insights into their mechanical properties and state inversion, potential refinements of the framework discussed in this study, and also state of practice procedures for New Zealand. This could be conducted using mini calibration chambers (e.g., Ref. [41–43]), which would allow the generation of a significant amount of data.

7. Conclusions

Traditional approaches for assessing cyclic liquefaction triggering do not directly integrate mechanical properties like those often used in static liquefaction assessments. This study discussed a framework that bridges this gap. Ingredients of the discussed framework are (1) the measurement (typically through triaxial tests) or estimation (e.g., from CPTu data) of mechanical properties (i.e., $G_{max}, M_{tc}, N, H, \chi, \Gamma, \lambda$), (2) an inversion procedure to retrieve ψ from CPTu measurements that provide k and m inversion coefficients, (3) a $CRR - \psi$ liquefaction curve, and (4) the representation of the seismic demand through *CSR*. Even with general considerations informed by CSSM principles for estimating mechanical properties of Christchurch soils, the discussed framework showed comparable performance to that of the Boulanger and Idriss [18] procedure, which has been calibrated with New Zealand Liquefaction case histories. This was the case when the proposed cavity expansion, Mozaffari and Ghafghazi [46], or Robertson [40] inversions are used. This result is encouraging as it opens avenues for a more active integration of mechanics into liquefaction engineering. Notably, the inversion procedures recommended for New Zealand can be used with

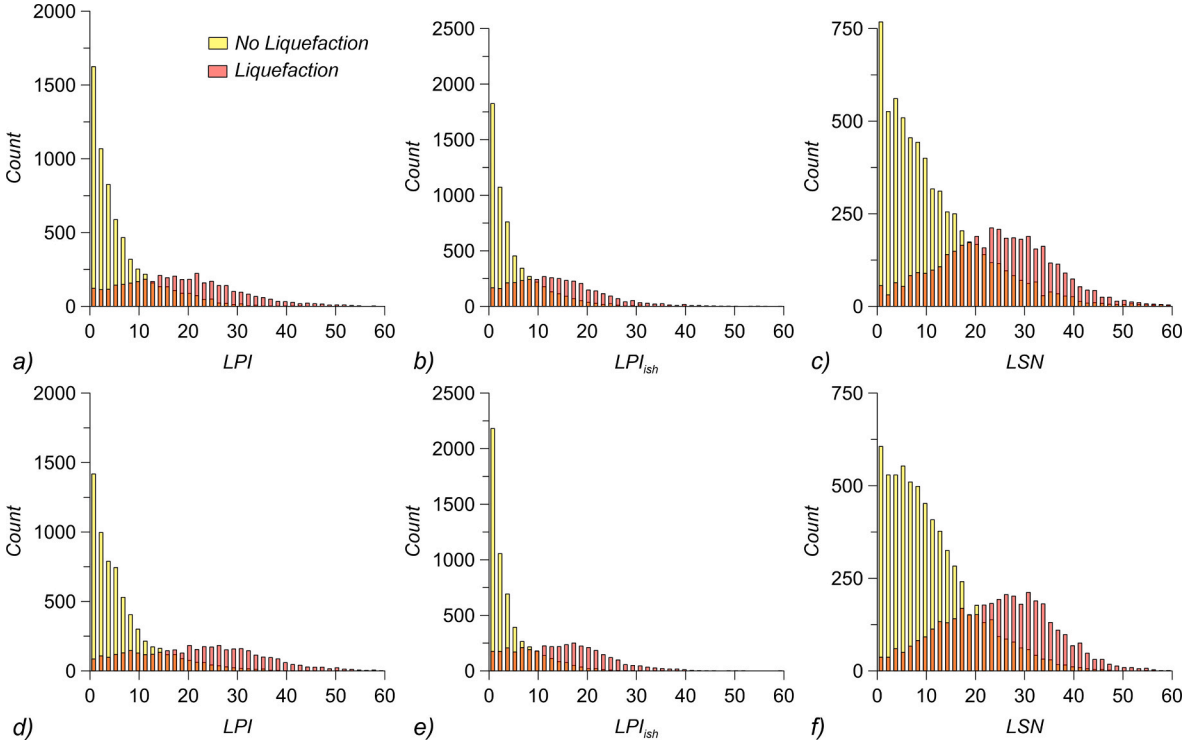

Fig. 12. Histograms of liquefaction and non-liquefaction manifestations considering for *LPI* (left column), LPI_{ish} (middle column) and *LSN* (left column) for R10 (a to c), and the calibrated cavity expansion in this study (d to f).

inputs comparable to standard procedures, i.e., CPTu information and a seismic demand assessment – often provided by probabilistic seismic hazard assessment. The framework assessment also revealed that the Shuttle and Jefferies [35], Ghafghazi and Shuttle [44], Been and Jefferies [39], and Plewes et al. [38] inversion procedures produce quite low LSI (i.e., *LPI*, LPI_{ish}, and *LSN*) values; hence, they are unconservative in the context of the database used in this study and are not recommended.

The discussed framework addresses the limitations of state-of-practice approaches developed mainly for sands or silty sands, with the bulk of data having FC<~35, which put significant weight on fine contents correction, but, in the authors view, without a fundamental basis. Conversely, CSSM, the basis for the discussed framework, uses the same equations across the spectrum from soft clay through to (at least) coarse sand, replacing the FC concept (and associated corrections) with the soil's intrinsic friction (e.g., M_{tc}) and its compressibility (e.g., λ_e). CSSM departs from the 'sand-like' or 'clay-like' concepts commonly used in practice, as different soils simply exhibit different mechanical properties (e.g., M_{tc}, λ_e). Thus, it can be accommodated for different soils as far as adequate mechanical properties are considered. Moreover, it accommodates stress and density dependence inherently. Going back to the recommended inversion procedures in this study, conceptually, they can be regarded as "ergodic" (e.g. Ref. [65], discusses ergodicity concepts), as they have been assessed considering an average scaling of mechanical properties for the considered New Zealand database. This is similar to state-of-the-practice procedures, which are also average models. An important feature of the discussed framework is that it facilitates the transition to non-ergodic (i.e., region or site-specific) liquefaction assessments while promoting the integration of additional mechanistic concepts. This means that the steps of the discussed framework could be applied in future efforts to other broad or localized regions (e.g., the areas affected by the recent Kahramanmaraş Earthquake Sequence in Turkey) as far as information is available. This resembles the transition from ergodic to non-ergodic ground motion models in earthquake engineering (e.g., Ref. [66]).

Last, in terms of potential future efforts, without changing the "essence" of the discussed framework, there is potential for refinements considering (1) additional data; for example, the recent Kahramanmaraş Earthquake Sequence in Turkey is expected to provide significant data, (2) region-dependent inversion procedures, and (3) incorporating a suite of $CRR - \psi$ and "true-liquefaction" curves, expected to be a function of λ based on CSSM.

CRediT authorship contribution statement

Jorge Macedo: Conceptualization, Funding acquisition, Methodology, Project administration, Resources, Supervision, Validation, Writing – original draft, Writing – review & editing. **Luis Vergaray:** Data curation, Formal analysis, Validation, Visualization, Writing – original draft.

Declaration of competing interest

The authors declare that they have no known competing financial interests or personal relationships that could have appeared to influence the work reported in this paper.

Data availability

Data will be made available on request.

Acknowledgements

This material is based upon work supported by the National Science Foundation (NSF) under the Grant No. CMMI 2145092. Any opinions, findings, conclusions, or recommendations expressed in this material are those of the author(s) and do not necessarily reflect the views of the National Science Foundation. The PRONABEC program of the Peruvian government provided additional financial support. Finally, the authors thank Juan C. Tarazona for his help in managing and processing the data.

Appendix A. Supplementary data

Supplementary data to this article can be found online at https://doi.org/10.1016/j.soildyn.2024.108520.

References

[1] Morgenstern N, Vick S, Viotti C, Watts B. Fundão tailings dam review panel report on the immediate causes of the failure of the Fundão dam. New York: Cleary Gottlieb Steen and Hamilton LLP; 2016.
[2] Robertson PK, de Melo L, Williams DJ, Wilson GW. Report of the expert panel on the technical causes of the failure of Feijão Dam I. 2019.
[3] France J, Irfan A, Miller A, Williams J, Higinbotham S. "Investigation of failures of Edenville and sanford dams." independent forensic team – final report. Available at: https://damsafety-prod.s3.amazonaws.com/s3fs-public/files/Edenville-Sanford_Final%20Report_Main%20Report%20and%20Appendices.pdf; 2022.
[4] Geotechnical Extreme Events Reconnaissance, GEER. "Geotechnical reconnaissance of the 2010 Darfield (New Zealand) earthquake." - report GEER-024 prepared by green, R., cubrinovski, M. 2010. https://doi.org/10.18118/G6D59F.
[5] Geotechnical Extreme Events Reconnaissance, GEER. "Geotechnical reconnaissance of the 2011 Christchurch, New Zealand earthquake" - report GEER-027 prepared by duman E., lozano, J., nichols, E. 2011. https://doi.org/10.18118/G68G65.
[6] Geotechnical Extreme Events Reconnaissance GEER. "Turkey earthquake virtual report on geotechnical impacts." - report GEER-082 prepared by Duman E., Lozano. J., Nichols, E; 2023. https://doi.org/10.18118/G6T951.
[7] Cubrinovski M, Bradley B, Wotherspoon L, Green R, Bray J, Wood C, Pender M, Allen J, Bradshaw A, Rix G, Taylor M, Robinson K, Henderson D, Giorgini S, Ma K, Winkley A, Zupan J, O'Rourke T, DePascale G, Wells D. Geotechnical aspects of the 22 february 2011 Christchurch earthquake. Bull N Z Soc Earthq Eng 2011;44(4):205–26. https://doi.org/10.5459/bnzsee.44.4.205-226.
[8] Bray J, Cubrinovski M, Zupan J, Taylor M. Liquefaction effects on buildings in the central business district of Christchurch. Earthq Spectra 2014;30(1):85–109. https://doi.org/10.1193/022113eqs043m.
[9] van Ballegooy S, Malan P, Lacrosse V, Jacka ME, Cubrinovski M, Bray JD, O'Rourke TD, Crawford SA, Cowan H. Assessment of liquefaction-induced land damage for residential Christchurch. Earthq Spectra 2014;30(1):31–55. https://doi.org/10.1193/031813eqs070m.
[10] Green RA, Cubrinovski M, Bradley B, Henderson D, Kailey P, Robinson K, Taylor M, Winkley A, Wotherspoon L, Orense R, Pender M, Hogan L, Allen J, Bradshaw A, Bray J, DePascale G, O'Rourke T, Rix G, Wells D, Wood C. Geotechnical aspects of the Mw 6.2 2011 Christchurch, New Zealand, earthquake. GeoCongress 2012; 2012. https://doi.org/10.1061/9780784412121.175.
[11] Wotherspoon L, Bradshaw A, Green R, Wood C, Palermo A, Cubrinovski M, Bradley B. Performance of bridges during the 2010 Darfield and 2011 Christchurch earthquakes. Seismol Res Lett 2011;82(6):950–64. https://doi.org/10.1785/gssrl.82.6.950.
[12] Lyman. Construction of franklin falls dam. Report, US Army Corps of Engineers; 1938.
[13] Morgenstern NR, Jefferies M, Zyl DV, Wates J. "Independent technical review board." report on NTSF embankment failure. 2019.
[14] Seed HB, Idriss IM. Simplified procedure for evaluating soil liquefaction potential. ASCE J. Soil Mech Found. Div. 1971. https://doi.org/10.1061/jsfeaq.0001662.
[15] Whitman RV. Resistance of soil to liquefaction and settlement. Soils Found 1971. https://doi.org/10.3208/sandf1960.11.4_59.
[16] Seed HB, Idriss I. Ground motions and soil liquefaction during earthquakes. Earthquake Engineering Research Institute; 1982.
[17] Boulanger RW, Idriss IM. Probabilistic standard penetration test-based liquefaction-triggering procedure. J Geotech Geoenviron Eng 2012. https://doi.org/10.1061/(asce)gt.19435606.0000700.
[18] Boulanger RW, Idriss IM. CPTbased liquefaction triggering procedure. J Geotech Geoenviron Eng 2016. https://doi.org/10.1061/(asce)gt.19435606.0001388.
[19] Robertson PK, Wride CE. Evaluating cyclic liquefaction potential using the cone penetration test. Can Geotech J 1998. https://doi.org/10.1139/t98017.
[20] Been K, Jefferies MG. A state parameter for sands. Geotechnique 1985. https://doi.org/10.1680/geot.1985.35.2.99.
[21] Iwasaki TF, Tatsuoka K, Yasuda ST. A practical method for assessing soil liquefaction potential based on case studies at various sites in Japan. In: Proc, 7th world conference on earthquake engineering, istanbul, Turkey; 1978.
[22] Iwasaki T, Arakawa T, Tokida K. Simplified procedures for assessing soil liquefaction during earthquakes. In: Proceedings of the conference on soil dynamics and earthquake engineering. Southampton; 1982. p. 925–39.
[23] Maurer BW, Green RA, O. Taylor S. Moving towards an improved index for assessing liquefaction hazard: lessons from historical data. Soils Found 2015;55(4):778–87. https://doi.org/10.1016/j.sandf.2015.06.010.

[24] van Ballegooy S, Malan PJ, Jacka ME, Lacrosse VIMF, Leeves JR, Lyth JE, Cowan H. Methods for characterising effects of liquefaction in terms of damage severity. In: Proc., 15th; 2012.
[25] Upadhyaya S, Green RA, Maurer BW, Rodriguez-Marek A, van Ballegooy S. Limitations of surface liquefaction manifestation severity index models used in conjunction with simplified stressbased triggering models. J Geotech Geoenviron Eng 2022;148(3):04021194. https://doi.org/10.1061/(ASCE)GT.1943-5606.0002725.
[26] Maurer BW, Green RA, Cubrinovski M, Bradley B. Calibrating the liquefaction severity number (LSN) for varying mispredict ion economies: a case Study in Christchurch, New Zealand. In: Proc., 6th int. Conf. On earthquake geotechnical engineering. London: International Society of Soil Mechanics and Geotechnical Engineering; 2015.
[27] Tonkin, Taylor. Liquefaction vulnerability study. In: Report to earthquake commission, ref.52020.0200/v1.0. Christchurch, New Zealand: Tonkin and Taylor; 2013.
[28] Upadhyaya S, Maurer BW, Green RA, Rodriguez-Marek A. Effect of non-liquefiable high fines-content, high plasticity soils on liquefaction potential index (LPI) performance. In: Geotechnical earthquake engineering and soil dynamics V: liquefaction triggering, consequences, and mitigation. vol. 290. ASCE Geotechnical Special Publication; 2018. p. 191–8.
[29] Upadhyaya S, Maurer BW, Green RA, Rodriguez-Marek A, van Ballegooy S. Surficial liquefaction manifestation severity thresholds for profiles having high fines-content, high plasticity soils. Can Geotech J 2022. https://doi.org/10.1139/cgj-2022-0092.
[30] Jefferies M, Been K. Soil Liquefaction: a critical state approach. second ed. (second ed. CRC Press; 2015. https://doi.org/10.1201/b19114.
[31] Youd TL, Idriss IM. Liquefaction resistance of soils: summary report from the 1996 NCEER and 1998 NCEER/NSF workshops on evaluation of liquefaction resistance of soils. J Geotech Geoenviron Eng 2001;127(4):297–313. https://doi.org/10.1061/(asce)1090-0241(2001)127:4(297).
[32] Macedo J, Vergaray L. Properties of mine tailings for static liquefaction assessment. Can Geotech J 2022;59(5):667–87. https://doi.org/10.1139/cgj-2020-0600.
[33] Vergaray L, Macedo J, Arnold C. Static and cyclic liquefaction of copper mine tailings. J Geotech Geoenviron Eng 2023;149(5). https://doi.org/10.1061/jggefk.gteng-10661.
[34] Jefferies M. On the fundamental nature of the state parameter. Geotechnique 2022; 72(12):1082–91. https://doi.org/10.1680/jgeot.20. 228.
[35] Shuttle D, Jefferies M. Dimensionless and unbiased CPT interpretation in sand. Int J Numer Anal Methods GeoMech 1998;22(5):351–91.
[36] Been K, Crooks J, Becker D, Jefferies M. The cone penetration test in sands: part I, state parameter interpretation. Geotechnique 1986;36(2):239–49.
[37] Been K, Jefferies M, Crooks J, Rothenburg L. A critical appraisal of CPT calibration chamber tests. Proc. 1st Int.Symposium Penetrat. Test. (ISOPT) 1988;2:651–60.
[38] Plewes HD, Davies MP, Jefferies MG. CPT based screening procedure for evaluating liquefaction susceptibility. In: Proceedings of the 45th Canadian geotechnical conference; 1992. p. 41–9.
[39] Been K, Jefferies MG. Towards systematic CPT interpretation. Predictive soil mechanics; 1992. p. 121–34. https://doi.org/10.1680/psm.19164.0008.
[40] Robertson PK. Evaluation of flow liquefaction and liquefied strength using the cone penetration test. J. Geotech. Geoenviron. Eng., ASCE 2010;136(6):842–53. https://doi.org/10.1061/(ASCE)GT.1943-5606.0000286.
[41] Franzen JH. Cone penetration resistance in silt. In: M.Sc. Thesis. University of Rhode Island; 2006.
[42] Kokusho T, Nakashima S, Kubo A, Ikeda K. Soil investigation of fly ash deposit improved by heavy compaction method. J Geotech Geoenviron Eng 2012;138(6): 738–46.
[43] Damavandi-Monfared S, Sadrekarimi A. Development of a miniature cone penetrometer for calibration chamber testing. Geotech Test J 2015;38(6): 20150036.
[44] Ghafghazi M, Shuttle D. Interpretation of sand state from cone penetration resistance. Geotechnique 2008;58(8):623–34. https://doi.org/10.1680/geot.2008.58.8.623.
[45] Shuttle D, Jefferies M. Determining silt state from CPTu. Geotechn. Res. 2016;3(3): 90–118. https://doi.org/10.1680/jgere.16.00008.
[46] Mozaffari M, Ghafghazi M. Material-specific interpretation of the state parameter from drained cone penetration test. Can Geotech J 2023. https://doi.org/10.1139/cgj-2022-0490.
[47] Robertson PK. Soil classification using the cone penetration test. Can Geotech J 1990;27(1):151–8.
[48] Macedo J, Vergaray L, Jensen C, Cornejo R, Jefferies M. Harbor Bay business park liquefaction during loma Prieta earthquake - a critical state perspective. Soil Dynam Earthq Eng 2022;158:107280. https://doi.org/10.1016/j.soildyn.2022.107280.
[49] Upadhyaya S, Green RA, Rodriguez-Marek A, Maurer BW. True liquefaction triggering curve. J Geotech Geoenviron Eng 2023;149(3). https://doi.org/10.1061/jggefk.gteng-11126.
[50] Moss R. CPT-based probabilistic assessment of seismic soil liquefaction initiation. Berkeley: Ph.D. Dissertation, University of California; 2003.
[51] Geyin M, Maurer BW, Bradley BA, Green RA, van Ballegooy S. CPT-based liquefaction case histories compiled from three earthquakes in Canterbury," New Zealand. Earthq Spectra 2021;37(4):2920–45. https://doi.org/10.1177/8755293021996367.
[52] Bradley BA. Site-specific and spatially-distributed ground motion intensity estimation in the 2010-2011 Christchurch earthquakes. Soil Dynam Earthq Eng 2014;48:35–47.
[53] Green RA, Cubrinovski M, Cox B, Wood C, Wotherspoon L, Bradley B, Maurer B. Select liquefaction case histories from the 2010-2011 Canterbury earthquake sequence. Earthq Spectra 2014;30(1):131–53.
[54] Maurer BW, Green RA, Cubrinovski M, Bradley B. Assessment of CPT-based methods for liquefaction evaluation in a liquefaction potential index framework. Geotechnique 2015;65(5):328–36. https://doi.org/10.1680/geot.SIP.15.P.007.
[55] Maurer BW, Green RA, Cubrinovski M, Bradley B. Fines-content effects on liquefaction hazard evaluation for infrastructure in Christchurch, New Zealand. Soil Dynam Earthq Eng 2015;76(Sep):58–68. https://doi.org/10.1016/j.soildyn.2014.10.028.
[56] Maurer BW, Green RA, van Ballegooy S, Bradley BA, Upadhyaya S. Performance comparison of probabilistic and deterministic liquefaction triggering models for hazard assessment in 23 global earthquakes. In: Huang J, Fenton GA, Zhang L, Griffiths DV, editors. Geo-risk 2017: reliability-based design and code developments, ASCE geotechnical special publication 283; 2017. p. 31–42.
[57] Maurer BW, Green RA, van Ballegooy S, Wotherspoon L. Assessing liquefaction susceptibility using the CPT soil behavior type index. In: Proc., 3rd int. Conf. On performance-based design in earthquake geotechnical engineering (PBDIII). London: International Society of Soil Mechanics and Geotechnical Engineering; 2017.
[58] Fawcett T. An introduction to ROC analysis. Pattern Recogn Lett 2006. https://doi.org/10.1016/j.patrec.2005.10.010.
[59] Green R, Upadhyaya S, Wood C, Maurer B, Cox B, Wotherspoon L, Bradley B, Cubrinovski M. Relative efficacy of CPT- versus Vs-based simplified liquefaction evaluation procedures. Proc. 19th Intern. Conf. Soil Mechan Geotechn.Eng. 2017: 1521–4.
[60] Geyin M, Baird AJ, Maurer B. Field assessment of liquefaction prediction models based on geotechnical vs. geospatial data, with lessons for each. Earthq Spectra 2020;36(3):1386–411.
[61] Robertson PK, Cabal KL. "Estimating soil unit weight from CPT". Huntington Beach, CA, USA: 2nd International Symposium on Cone Penetration Testing; 2010.
[62] Maurer BW, Green RA, van Ballegooy S, Wotherspoon L. Development of region-specific soil behavior type index correlations for evaluating liquefaction hazard in Christchurch, New Zealand. Soil Dynam Earthq Eng 2019;117(Feb):96–105. https://doi.org/10.1016/j.soildyn.2018.04.059.
[63] McGann CR, Bradley BA, Taylor ML, Wotherspoon LM, Cubrinovski M. Development of an empirical correlation for predicting shear wave velocity of Christchurch soils from cone penetration test data. Soil Dynam Earthq Eng 2015; 75:66–75. https://doi.org/10.1016/j.soildyn.2015.03.023.
[64] Reid D. Estimating slope of critical state line from cone penetration test — an update. Can Geotech J 2015;52(1):46–57. https://doi.org/10.1139/cgj-2014-0068.
[65] Rodriguez-Marek A, Cotton F, Abrahamson N, Akkar S, Al Atik L, Edwards B, Montalva G, Dawood H. A model for single-station standard deviation using data from various tectonic regions. Bull Seismol Soc Am 2013;103(6):3149–63.
[66] Macedo J, Liu C, Kottke A. "Evaluating the performance of non-ergodic ground motion models in the ridgecrest area". Georisk 2023:203–13.